ACS APPLIED MATERIALS & INTERFACES

www.acsami.org

Research Article

Damping and Interfacial Dzyaloshinskii–Moriya Interaction in Thulium Iron Garnet/Bismuth-Substituted Yttrium Iron Garnet Bilayers

Takian Fakhrul,[‖] Bharat Khurana,[‖] Byung Hun Lee, Siying Huang, Hans T. Nembach, Geoffrey S. D. Beach, and Caroline A. Ross*

Cite This: https://doi.org/10.1021/acsami.3c14706

Read Online

ACCESS | Metrics & More | Article Recommendations

ABSTRACT: Thin films of ferrimagnetic iron garnets can exhibit useful magnetic properties, including perpendicular magnetic anisotropy (PMA) and high domain wall velocities. In particular, bismuth-substituted yttrium iron garnet (BiYIG) films grown on garnet substrates have a low Gilbert damping but zero Dzyaloshinskii–Moriya interaction (DMI), whereas thulium iron garnet (TmIG) films have higher damping but a nonzero DMI. We report the damping and DMI of thulium-substituted BiYIG (BiYTmIG) and TmIG|BiYIG bilayer thin films deposited on (111) substituted gadolinium gallium garnet and neodymium gallium garnet (NGG) substrates. The films are epitaxial and exhibit PMA. BiYIG|TmIG bilayers have a damping value that is an order of magnitude lower than that of TmIG, and BiYIG|TmIG|NGG have DMI of 0.0145 ± 0.0011 mJ/m^2, similar to that of TmIG|NGG. The bilayer therefore provides a combination of DMI and moderate damping, useful for the development of high-speed spin orbit torque-driven devices.

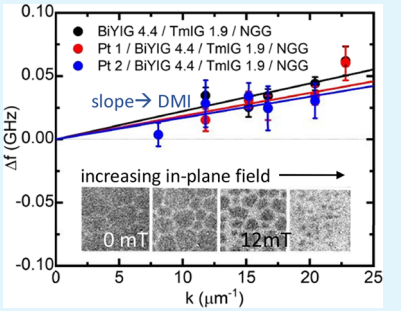

KEYWORDS: *spintronics, magnetism, damping, garnets, interfaces, thin films*

INTRODUCTION

Magnetically ordered oxide materials, such as spinels, ferrites,[1,2] and rare earth iron garnets[3−5] (REIGs) have been studied intensely for spintronic and photonic devices. In REIGs, the choice of rare earth (or other) ion allows tuning of a variety of properties, including saturation magnetization, compensation temperature,[6,7] magnetocrystalline anisotropy,[8] magnetostriction,[9] and Gilbert damping.[10,11] Magnetoelastic anisotropy can be introduced via lattice mismatch strain in epitaxial films or thermal mismatch strain for films grown on silicon or other nongarnet substrates,[12,13] and growth-induced anisotropy can be present in REIGs with mixed RE ions.[14,15]

Thin films of a number of REIGs have been grown with perpendicular magnetic anisotropy (PMA),[16−18] which is advantageous for the study of spin orbit torque (SOT) and other magnetic phenomena. REIGs are good insulators, enabling lower ohmic losses than metallic ferromagnets as they avoid parasitic current shunting from a metal overlayer.[19] PMA in epitaxial REIGs can be present even for thick films, as it originates from bulk anisotropy terms unlike the interfacial anisotropy dominating metallic ferromagnet films.[14,19] Thulium iron garnet ($Tm_3Fe_5O_{12}$ (TmIG))/heavy metal (HM) stacks grown epitaxially on gallium garnet substrates are the most extensively studied PMA REIG films in terms of their spintronic properties.[20−24] TmIG|Pt heterostructures exhibit considerable spin transparency at the interface, comparable to that of the Co|Pt interface,[16,25] and current induced switching of TmIG has been demonstrated using the damping-like SOT from a Pt overlayer.[22,26−28]

The Dzyaloshinskii–Moriya interaction (DMI) plays an important role in the stabilization and current-driven manipulation of chiral magnetic textures including Néel domain walls and skyrmions, which have been proposed to represent bits in data storage devices.[29,30] Key ingredients to obtain interfacial DMI are a broken inversion symmetry at the interface[27] and spin–orbit coupling.[31] While the HM overlayer contributes some spin–orbit coupling,[32] it appears that the RE^{3+} ions provide a critical contribution to DMI,[26] evident from the observation of DMI-stabilized skyrmions in TmIG grown on $Gd_3Ga_5O_{12}$ (GGG) in the absence of any HM overlayer[24] and the absence of DMI in bismuth-substituted yttrium iron garnet (BiYIG) (an iron garnet that does not have strong spin–orbit coupling due to the absence of RE^{3+} ions) with a HM overlayer.[26] The DMI in TmIG|Pt heterostructures stabilizes chiral Néel domain walls, which can be translated by

Received: October 2, 2023
Revised: December 8, 2023
Accepted: December 21, 2023

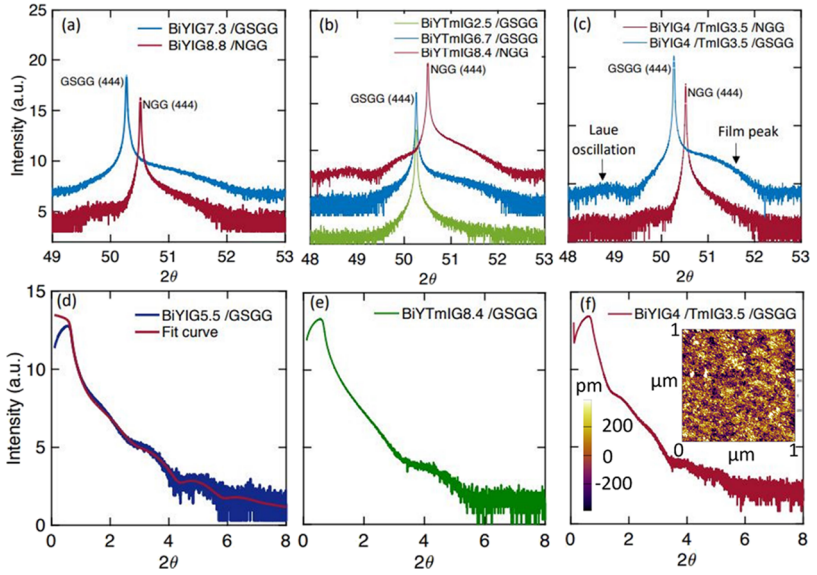

Figure 1. (a–c) High-resolution X-ray diffraction (HRXRD) scans of BiYIG, BiYTmIG, and BiYIG|TmIG thin films deposited on GSGG and NGG substrates. (d–f) X-ray reflectivity (XRR) scans of BiYIG, BiYTmIG, and BiYIG|TmIG thin films deposited on the GSGG substrate. A BiYIG/TmIG shot ratio of 25:5 was used for making the 2.5 nm thick BiYTmIG film and 25:2 was used for the 6.7 and 8.4 nm thick BiYTmIG films. Inset of (f) shows topographic image from an atomic force microscopy (AFM) scan on BiYIG (3.5 nm)/TmIG (3.1 nm)/GSGG film.

SOT produced by a charge current in the Pt overlayer without application of any in-plane field.[26] The strength of DMI for TmIG films varies with the substrate composition and has a nonmonotonic dependence on lattice mismatch strain, reaching 0.029 mJ m^{-2}.[33,34]

Gilbert damping governs the magnetization dynamics, including the critical current required for magnetization reversal in spin-transfer-torque devices[35,36] and the domain wall velocity for racetrack memory devices.[37] Yttrium iron garnet ($Y_3Fe_5O_{12}$, YIG) has the lowest known Gilbert damping, as low as 10^{-5} in bulk.[10,38,39] However, the growth of high-quality YIG films with PMA has been challenging, despite several demonstrations of epitaxial[40−42] and polycrystalline[43] PMA YIG films. Instead, epitaxial BiYIG can be grown with PMA on garnet substrates with higher lattice parameters than GGG by exploiting a combination of magnetoelastic and growth-induced anisotropies.[44,45] The Gilbert damping of BiYIG films is 1.3×10^{-4}–5.6×10^{-4}, an order of magnitude higher than that of YIG but much lower than that of REIGs with strong spin−orbit coupling.[10−12,14,44] For example, the damping of TmIG films is around 0.02.[20,23,46] While the low damping of BiYIG films enables fast domain wall dynamics, BiYIG films exhibit no DMI and SOT-driven domain wall motion can be achieved only in the presence of an in-plane magnetic field.[26,47]

Garnet thin films with DMI, low damping, and PMA would combine the advantages of fast dynamics and field-free SOT switching and bring substantial benefits to spintronics device development. In this article, we introduce a bilayer BiYIG|TmIG, which exhibits both DMI and moderate damping. Velez et al. described an exchange-coupled YIG|TmIG|Pt heterostructure,[48] demonstrating DMI-stabilized skyrmions, but the PMA was present only in the TmIG layer and the damping was not reported. There have also been various studies on multilayers of iron garnets for photonic and magneto-optic applications[49,50] but DMI and damping are not reported. Here, we report the growth and the structural, magnetic, and spintronic properties of BiYIG|TmIG heterostructures deposited on substituted gadolinium gallium garnet (GSGG) and neodymium gallium garnet (NGG) substrates. The films have PMA, and bubble domains in BiYIG|TmIG|GSGG were formed by applying simultaneous in-plane and out-of-plane fields. The key result of this work is showing that BiYIG|TmIG|NGG exhibits both a substantial DMI and damping an order of magnitude lower than that of TmIG.

STRUCTURAL AND MAGNETIC CHARACTERIZATION

The $Bi_{0.8}Y_{2.2}Fe_5O_{12}$ target was prepared by solid-state sintering, and the TmIG target was purchased from Furuuchi Chemical Corporation. Thin films of BiYIG, codeposited films of $(Tm,Bi,Y)_3Fe_5O_{12}$ (BiYTmIG) and bilayered films of TmIG|BiYIG were deposited on GSGG ($Gd_3Sc_2Ga_3O_{12}$, lattice parameter a = 1.2554 nm) and NGG ($Nd_3Ga_5O_{12}$, a = 1.2505 nm) substrates with (111) orientation using pulsed laser deposition (PLD) with a 248 nm wavelength laser. The BiYTmIG films were codeposited by alternately ablating the targets using 25 laser shots on the BiYIG target and 2 or 5 laser shots on the TmIG target. Based on the calibration of the growth rates from BiYIG and TmIG targets, the two codeposited BiYTmIG films have nominal compositions of $Tm_{0.15}Bi_{0.75}Y_{2.1}Fe_5O_{12}$ and $Tm_{0.3}Bi_{0.7}Y_2Fe_5O_{12}$, respectively. The bilayered films consisted of a TmIG layer in contact with the substrate and an overlaid BiYIG layer. Several studies show DMI originating from the TmIG|substrate interface,[33,34] thus stacks of BiYIG|TmIG|substrate were examined instead of TmIG|BiYIG|substrate. The optimized growth conditions for epitaxial high-quality BiYIG films are described in our previous work.[51] The growth conditions used in the present work can be found in the Methods section.

REIGs, YIG, and BiYIG belong to the cubic $Ia\bar{3}d$ space group[52] with a lattice parameter of about 1.2 nm, well matched to that of gallium garnets. Figure 1 shows symmetric high-resolution X-ray diffraction (HRXRD) scans around the (444) substrate peak for BiYIG, codeposited BiYTmIG, and bilayered TmIG|BiYIG films. All the films grow with an in-plane tensile

https://doi.org/10.1021/acsami.3c14706
ACS Appl. Mater. Interfaces XXXX, XXX, XXX−XXX

strain due to lattice mismatch with the substrates. Due to the few-nanometer film thickness, the intensity of the film peaks and Laue fringes is low, and the film peaks are very broad and overlap the substrate peaks. However, thicker epitaxial iron garnet films grown under similar conditions exhibit well-defined film peaks and Laue fringes, indicating high crystalline quality and thickness uniformity in epitaxial REIG films.[5,14,45] High-resolution X-ray reflectivity (HRXRR) measurements were performed to determine the film thickness, as shown in Figure 1. Fits to the Kiessig fringes in HRXRR scans for BiYIG and BiYTmIG films deposited on a GSGG substrate indicate uniform thicknesses of 5.5 and 8.4 nm, respectively. The observation of two distinct periodicities in the HRXRR scan for the bilayered film validates that the BiYIG layer and TmIG layer are not intermixed. Fits to the Kiessig fringes for the bilayered film indicate that the thicknesses of the BiYIG layer and TmIG layer are 4 and 3.5 nm, respectively. Prior work has shown, based on reciprocal space map measurements performed on BiYIG,[45] TmIG,[21] and terbium iron garnet (TbIG)[11] epitaxial films deposited on garnet substrates, that such garnet films are fully strained in-plane to match the substrate lattice parameter for the thickness of 70, 20, and 90 nm, respectively. Since all the BiYIG films, bilayered films, and codeposited films used in this study have thicknesses lower than 21 nm, we expect that they are all coherently lattice-matched to the substrate. Atomic force microscopy (AFM) measurements were performed on a BiYIG (3.5 nm)/TmIG (3.1 nm)/GSGG film and its rms surface roughness was 0.2 nm as shown in the inset of Figure 1f.

The uniaxial magnetic anisotropy K_u is defined as the magnetic energy difference between orienting the magnetization direction in-plane (E_{IP}) vs out-of-plane (E_{OOP}). Positive (negative) K_u implies an out-of-plane (in-plane) easy axis. For an epitaxial iron garnet film lattice-matched to a garnet substrate with (111) orientation, K_u is given by[12]

$$K_u = E_{IP} - E_{OOP} = -\frac{K_1}{12} - \frac{\mu_0}{2}M_s^2 + \frac{9}{4}c_{44}\lambda_{111}\left(\frac{\pi}{2} - \beta\right) + K_G \quad (1)$$

Here, K_1 is the first-order cubic magnetocrystalline anisotropy constant, which is negative favoring PMA but is negligible compared to the other terms.[53] The second term is shape anisotropy with M_s the saturation magnetization, which favors an in-plane magnetization direction. The third term is the magnetoelastic anisotropy, which is proportional to magnetostriction λ_{111} and shear strain $(\pi/2 - \beta)$, with β being the corner angle of the rhombohedrally distorted unit cell. c_{44} is the shear modulus of the film and its value lies between 74 and 90 GPa for REIGs.[53] K_G, the fourth term, represents a uniaxial growth-induced anisotropy that originates from preferential occupancy of cations or vacancies in nonequivalent sites.[14,15,54,55] Surface and interface anisotropies[56] may also contribute to K_u.

All of the films in this study exhibited PMA. Vibrating sample magnetometry (VSM) hysteresis loops for representative bilayered films and codeposited films deposited on GSGG and NGG substrates are shown in Figure 2. The measurement with an out-of-plane field shows square hysteresis loops and a low coercivity of less than 400 A/m. The large paramagnetic nonlinear signal of the GSGG and NGG substrates prevented background subtraction for the in-plane hysteresis loops of the films. The saturation magnetization of these films is in the range of 80−105 kA/m at room temperature, comparable to TmIG (90−120 kA/m)[21,57] and BiYIG films (125−145 kA/m).[45] Both BiYIG[58] and TmIG[21] have negative λ_{111} and an in-plane tensile strain so that the magnetoelastic anisotropy favors PMA. Additionally, the growth-induced anisotropy due to preferential occupancy of cations in nonequivalent dodecahedral sites favors PMA in BiYIG,[44,45] and likely also contributes to the anisotropy of the BiYTmIG codeposited film.

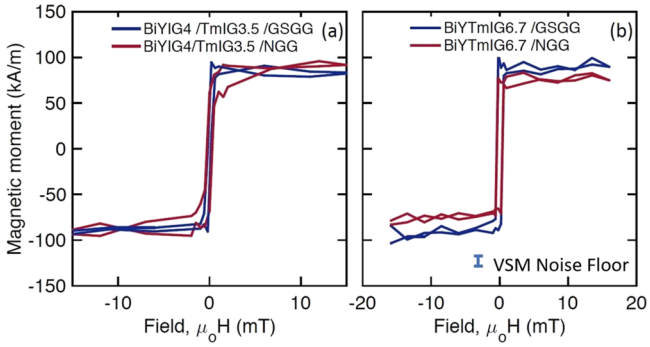

Figure 2. Room-temperature out-of-plane vibrating sample magnetometry hysteresis loops of (a) BiYIG (4 nm)|TmIG (3.5 nm) and (b) BiYTmIG (6.7 nm) thin films deposited on GSGG and NGG substrates. A BiYIG/TmIG shot ratio of 25:2 was used for BiYTmIG films.

MEASUREMENTS OF DAMPING

The damping was measured using broadband perpendicular ferromagnetic resonance (FMR) spectroscopy with a vector network analyzer (VNA) in the frequency range of 10−40 GHz.[59−62] The complex transmission parameter S_{21} was measured at a particular frequency as the magnetic field was swept.[59] Damping α of the films was obtained by fitting full width at half maximum (fwhm) linewidth ΔH to the following equation:

$$\Delta H = \frac{4\pi\alpha f}{|\gamma|\mu_0} + \Delta H_0 \quad (2)$$

ΔH is obtained by fitting the S_{21} data to the complex susceptibility as shown in Figure 3a. f is the excitation frequency, ΔH_0 is the inhomogeneous linewidth broadening, and γ is the gyromagnetic ratio given by $(g\mu_B)/\hbar$, where μ_B is the Bohr magneton, $\hbar$ is the reduced Planck's constant, and g is the Landé g-factor.

The linear fits obtained from $\Delta H(f)$ and the corresponding damping values for various bilayer and codeposited films are shown in Figure 3. The data for a 70 nm thick BiYIG film deposited on a GSGG substrate from our previous work has been included for comparison.[45] Damping and ΔH_0 values for bilayered and codeposited films from this study are displayed in Table I. The data obtained from the codeposited film show a less clear linear fit than that of the other films, but we nevertheless include its damping value in Table I. The damping of the bilayer films is between 5.2×10^{-3} and 7.6×10^{-3} with $\mu_0\Delta H_0$ of 4−9 mT. While these damping values are 1 order of magnitude higher than that of BiYIG,[44,45] they are still an order of magnitude lower than what has been reported for TmIG.[20,23,46] ΔH_0 values for TmIG/BiYIG bilayer films are also intermediate between those of BiYIG and TmIG. The codeposited BiYTmIG film, which contains a low fraction of Tm (with nominal composition of

https://doi.org/10.1021/acsami.3c14706
ACS Appl. Mater. Interfaces XXXX, XXX, XXX−XXX

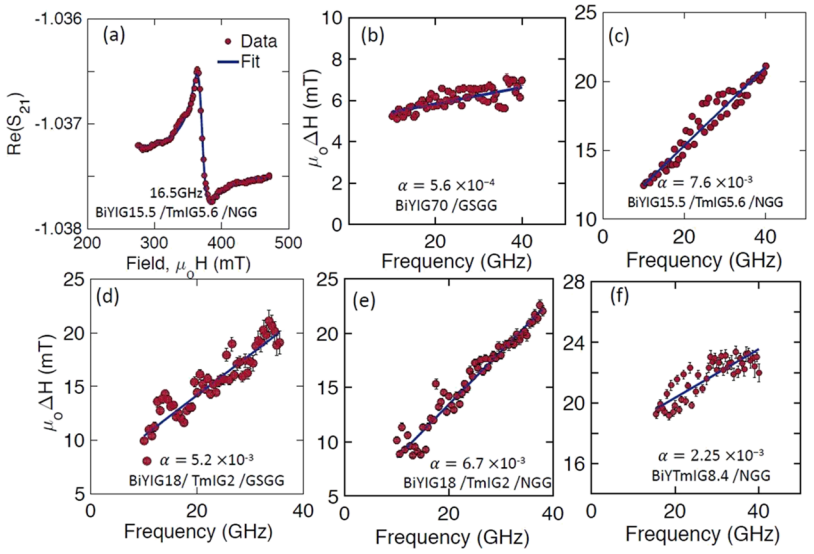

Figure 3. (a) Representative FMR spectrum taken at 16.5 GHz showing the real part of S_{21} for BiYIG (15.5 nm)/TmIG (5.6 nm)/NGG. Fits of linewidth, ΔH, as a function of frequency for (b) BiYIG (70 nm)/GSGG, (c) BiYIG (15.5 nm)/TmIG (5.6 nm)/NGG, (d) BiYIG (18 nm)/TmIG (2 nm)/GSGG, (e) BiYIG (18 nm)/TmIG (2 nm)/NGG, and (f) BiYTmIG (8.4 nm)/NGG with BiYIG/TmIG shot ratio of 25:2.

Table I. Gilbert Damping and *D* Values for Various Films

stack	K_u (kJ/m^3)	Gilbert damping	inhomogeneous linewidth broadening $\mu_0\Delta H_0$ (mT)	D (mJ m^{-2})
BiYIG (70 nm)/GSGG	8.8 ± 0.7	5.6 ± 0.7 × 10^{-4}	5 ± 0.1	n/a
BiYIG (4.3 nm)/GSGG	n/a	n/a	n/a	0.001 ± 0.002
BiYIG(4.3 nm)/NGG	n/a	n/a	n/a	0.003 ± 0.002
Pt(1 nm)/BiYIG(4.3 nm)/NGG	n/a	n/a	n/a	0.003 ± 0.018
Pt(2 nm)/BiYIG(4.3 nm)/NGG	n/a	n/a	n/a	0.001 ± 0.001
BiYTmIG (8.4 nm)/NGG (BiYIG/TmIG shot ratio of 25:2)	8.6 ± 1.2	2.25 ± 0.2 × 10^{-3}	17 ± 0.5	n/a
BiYIG (15.5 nm)/TmIG (5.6 nm)/NGG	11.6 ± 1.6	7.6 ± 0.27 × 10^{-3}	9.2 ± 0.5	n/a
BiYIG (18 nm)/TmIG (2 nm)/GSGG	8.4 ± 1.1	5.2 ± 0.32 × 10^{-3}	6.6 ± 0.5	n/a
BiYIG (18 nm)/TmIG (2 nm)/NGG	5.7 ± 0.8	6.7 ± 0.21 × 10^{-3}	3.7 ± 0.4	n/a
BiYIG (4 nm)/TmIG (3.3 nm)/GSGG	n/a	n/a	n/a	0.001 ± 0.003
BiYIG (4.4 nm)/TmIG (1.9 nm)/NGG	4.6 ± 0.6	n/a	n/a	0.014 ± 0.002
Pt(1 nm)/BiYIG (4.4 nm)/TmIG (1.9 nm)/NGG	n/a	n/a	n/a	0.011 ± 0.003
Pt(2 nm)/BiYIG (4.4 nm)/TmIG (1.9 nm)/NGG	n/a	n/a	n/a	0.011 ± 0.001

$Tm_{0.15}Bi_{0.75}Y_{2.1}Fe_5O_{12}$) has damping between that of the bilayers and that of BiYIG, but its $\mu_0\Delta H_0$ is higher.

The resonance field was fitted to the Kittel equation for perpendicular geometry[59]:

$$H_{res} = \frac{2\pi f}{|\gamma|\mu_0} + M_{eff} \quad (3)$$

Here, H_{res} is the resonance field and M_{eff} is the effective magnetization. M_{eff} obtained from the fit was used to calculate the net anisotropy of these films K_u using the following equation:

$$K_u = \frac{-\mu_0 M_s M_{eff}}{2} \quad (4)$$

Calculated K_u values for various films are displayed in Table I. All the films have positive K_u values, indicating PMA in these films. This is consistent with the high remanence out-of-plane VSM hysteresis loops displayed in Figure 2.

MEASUREMENTS OF DMI

Brillouin light scattering (BLS) measurements[63−65] were performed at room temperature in the Damon−Eshbach geometry[66,67] with an in-plane field of 5 kOe perpendicular to the spin wave propagation direction. For the DE mode, DMI provokes nonreciprocity in the counter-propagating DE mode frequencies, with frequencies given by[65]

$$f_{DE}(\pm k) = f_0 \pm f_{DMI} = f_0 \pm \frac{\gamma D k}{\pi M_s} \quad (5)$$

where f_0 is the DE mode frequency in the absence of DMI, k is the wavevector of the spin wave, and D is the strength of the DMI. Then, the frequency difference between Stokes and anti-Stokes peaks, $\Delta f = f(k) - f(-k)$ is measured as a function of wavevector, k. The D values for various films from this study were obtained by least-squares fitting to $\Delta f = \frac{2\gamma D k}{\pi M_s}$ and are displayed in Table I.

Figure 4a,b indicates a lack of peak splitting and hence negligible DMI in BiYIG (4.3 nm)|GSGG and in BiYIG (4.3 nm)|NGG without a Pt overlayer and with a Pt overlayer of thickness 1 and 2 nm (their D values along with error bars displayed in Table I include the possibility that DMI is zero). These observations are consistent with prior results for BiYIG.[26] The paramagnetic substrates GSGG and NGG

https://doi.org/10.1021/acsami.3c14706
ACS Appl. Mater. Interfaces XXXX, XXX, XXX−XXX

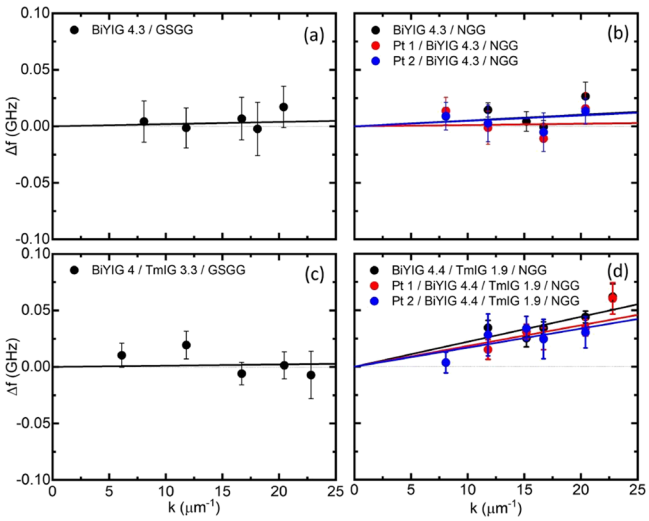

Figure 4. BLS frequency change Δf versus wavenumber k for (a) BiYIG (4.3 nm)/GSGG, (b) BiYIG (4.3 nm)/NGG, Pt (1 nm)/ BiYIG (4.3 nm)/NGG, Pt (2 nm)/ BiYIG (4.3 nm)/NGG, (c) BiYIG (4 nm)/TmIG (3.3 nm)/GSGG, and (d) BiYIG (4.4 nm)/TmIG (1.9 nm)/NGG, Pt (1 nm)/BiYIG (4.4 nm)/TmIG (1.9 nm)/NGG, Pt (2 nm)/BiYIG (4.4 nm)/TmIG (1.9 nm)/NGG.

contain rare earths Gd^{3+} ($4f^7$, $L = 0$) and Nd^{3+} ($4f^3$, $L = 6$), respectively, but neither BiYIG sample yields DMI. The importance of orbital angular momentum for obtaining DMI in REIG films has been noted,[26] but here the Gd^{3+} has no orbital moment and the Nd^{3+} in the NGG substrate may be ineffective in promoting DMI due to the paramagnetic host.

The BiYIG|TmIG|GSGG bilayer film has no DMI, Figure 4c, but BiYIG (4.4 nm)|TmIG (1.9 nm)|NGG without a Pt overlayer and with Pt of thickness 1 and 2 nm do exhibit DMI, Figure 4d, of $D = 0.0145 \pm 0.0011$ mJ/m^2. The critical D for stabilization of Néel domain walls is given by $(2t{\cdot}\ln(2)/\pi^2)\mu_0 M_s^2 = 0.010 \pm 0.003$ mJ/m^2, where t is the thickness of the magnetic layer and M_s is its saturation magnetization.[27] For BiYIG|TmIG|NGG this indicates that DMI is sufficient to stabilize the Néel domain walls.

Considering the inverse dependence of interfacial DMI on thickness, the measured DMI is comparable to that of TbIG|Pt deposited on GGG and TmIG|Pt deposited on $Gd_3Ga_5O_{12}$ (GGG), NGG, and SGGG (composition $Gd_{2.6}Ca_{0.4}Ga_{4.1}Mg_{0.25}Zr_{0.65}O_{12}$)[25,27,28,66] but an order of magnitude lower than that of metallic ferrimagnetic[68] and metallic ferromagnetic thin films.[69,70]

Introducing 1.9 nm TmIG at the interface results in a DMI of BiYIG|TmIG bilayers consistent with that of single layers of TmIG based on domain wall depinning measurements, where 6.6 nm TmIG|NGG had $D = 0.007 \pm 0.0015$ mJ m^{-2} but TmIG|GSGG had $D = 0.0015 \pm 0.002$ mJ m^{-2}.[34] Xu et al. also demonstrated a dependence of DMI strength on substrate composition in TmIG|Pt heterostructures.[33] The codeposited BiYTmIG films did not show a measurable DMI, likely due to their low Tm content.

The domain structure of bilayer films was examined using MOKE. An in-plane field was able to generate bubble domains at room temperature in Pt (4 nm)|BiYIG (4 nm)|TmIG (3.5 nm)|GSGG. Combinations of in-plane and out-of-plane fields were able to tune the bubble domain size over a wide range, as shown in Figure 5. The domains changed their sizes within small IP and OP field ranges indicating high domain wall mobility. Due to the low DMI for this sample, these bubble domains are unlikely to be DMI-stabilized skyrmions. We were unable to observe bubble domains in bilayered films deposited on NGG.

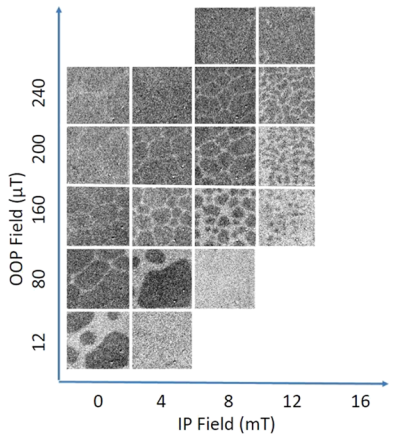

Figure 5. Domain structure of Pt (4 nm)/BiYIG (4 nm)/TmIG (3.5 nm)/GSGG for various values of in-plane field and out-of-plane field for a 100 μm × 100 μm area observed using MOKE microscope.

CONCLUSIONS

The Gilbert damping and DMI strength of epitaxial BiYIG, codeposited BiYTmIG, and bilayered BiYIG|TmIG films deposited on (111) GSGG and NGG substrates were investigated with the aim of identifying a path to develop films with low damping, high DMI and PMA. The films exhibit PMA with high remanence, attributed to magnetoelastic and growth-induced anisotropy, and show bubble domains with field-tunable size.

BiYIG|TmIG bilayers have a damping value 10× higher than that of BiYIG but 10× lower than that of single-layer TmIG. Additionally, their inhomogeneous linewidth broadening was lower than that reported for TmIG. BiYIG|TmIG|NGG has $D = 0.0145 \pm 0.0011$ mJ/m^2, but BiYIG|TmIG|GSGG had no DMI. This indicates a dependence of DMI strength on substrate composition, as seen for single-layer TmIG films where TmIG|NGG had higher DMI than TmIG|GSGG.[34] BiYIG|GSGG and BiYIG|NGG films had no DMI, which is consistent with other measurements. BiYIG|TmIG|NGG therefore provides a compromise, exhibiting PMA, DMI, and a damping that is an order of magnitude lower than that of TmIG. This work suggests that bilayers or multilayers of garnets provide opportunities to engineer combinations of magnetic properties that are not available from single-layer garnet films.

METHODS

Target fabrication, thin film deposition, and characterization: Precursor powders with the stoichiometric element ratios of the final target composition ($Bi_{0.8}Y_{2.2}Fe_5O_{12}$) were mixed and ball milled with yttrium stabilized zirconia grinding media for 24 h in ethanol. The mixture was then dried and calcined in a tube furnace in air to form the desired phase. Then, the calcinated powders were uniaxial and cold isostatic pressed at 40,000 psi for 2 min into a 1.1 in. diameter pellet. Finally, the pellet was transferred to a tube furnace and sintered to form the BiYIG target.

BiYIG, BiYTmIG, and TmIG|BiYIG films were grown by PLD on (111) oriented garnet substrates of the composition $Gd_3Sc_2Ga_3O_{12}$ (GSGG) and $Nd_3Ga_5O_{12}$ (NGG). The targets used for deposition had compositions of $Bi_{0.8}Y_{2.2}Fe_5O_{12}$ and $Tm_3Fe_5O_{12}$. Prior to

https://doi.org/10.1021/acsami.3c14706
ACS Appl. Mater. Interfaces XXXX, XXX, XXX−XXX

introducing oxygen and deposition of films, the chamber was pumped down to a 5×10^{-6} Torr base pressure. A laser repetition rate of 10 Hz, laser fluence of 2 J/cm^2, and target-substrate distance of 6 cm were used. For the TmIG|BiYIG bilayer growth, the O_2 pressure was 150 mTorr and the substrate temperature was 560 and 720 °C during the deposition of BiYIG and TmIG layers, respectively. For the codeposited BiYTmIG films, the O_2 pressure was 150 mTorr and the substrate temperature was 560 °C. An O_2 pressure of 230 Torr was maintained in the chamber as the samples cooled after growth.

An ultrahigh vacuum magnetron sputtering system with an Ar pressure of 2 mTorr was used for Pt deposition at room temperature. A Bruker D8 Discover HRXRD instrument was used to perform HRXRD measurements. An ADE 1660 VSM instrument was used to perform magnetic measurements. A custom-built, wide-field Kerr microscope with independent out-of-plane and in-plane magnetic field control was used to perform polar MOKE measurements to observe domains. Kohler illumination was adopted with an ×10 objective and a 456.6 nm wavelength LED light source.

FMR: The VNA technique was used to perform broadband perpendicular FMR spectroscopy. The samples were placed face-down on a 50 Ω coplanar waveguide. The films were saturated in the out-of-plane direction by sweeping an out-of-plane magnetic field up to $\mu_0 H = 2.2$ T. Microwave transmission over a frequency from 10 to 40 GHz was measured with a variable microwave field applied in-plane.

BLS: Due to the interfacial nature of DMI and its inverse dependence on film thickness, films with thicknesses lower than 10 nm were used for the BLS measurements, whereas thicker films were used for damping measurements by FMR. The BLS measurements were performed in backscattering geometry using a (3 + 3) tandem Fabry−Pérot interferometer and a 532 nm continuous-wave laser of 532 nm wavelength. The thermally generated Damon−Eshbach mode is measured with an in-plane applied field of 0.5 T. The wavevector of the DE mode is then determined by the angle θ between the film normal and incident laser, given by $k = \frac{4\pi}{\lambda}\sin\theta$. Each Stokes and anti-Stokes frequency is obtained from the Voigt fitting of the BLS spectra. Voigt fit and Lorentzian fit for the experimental data yield similar values for frequency, but the Voigt fit resulted in a lower error bar.

Certain commercial instruments are identified to adequately specify the experimental study. This does not imply endorsement by NIST or that the instruments are the best available for the purpose.

AUTHOR INFORMATION

Corresponding Author

Caroline A. Ross − *Department of Materials Science and Engineering, Massachusetts Institute of Technology, Cambridge, Massachusetts 02139, United States;* orcid.org/0000-0003-2262-1249; Email: caross@mit.edu

Authors

Takian Fakhrul − *Department of Materials Science and Engineering, Massachusetts Institute of Technology, Cambridge, Massachusetts 02139, United States*

Bharat Khurana − *Department of Materials Science and Engineering, Massachusetts Institute of Technology, Cambridge, Massachusetts 02139, United States;* orcid.org/0000-0001-5196-3817

Byung Hun Lee − *Department of Materials Science and Engineering, Massachusetts Institute of Technology, Cambridge, Massachusetts 02139, United States;* orcid.org/0000-0002-9804-8568

Siying Huang − *Department of Materials Science and Engineering, Massachusetts Institute of Technology, Cambridge, Massachusetts 02139, United States;* orcid.org/0000-0002-9108-7791

Hans T. Nembach − *Associate, Physical Measurement Laboratory, National Institute of Standards and Technology, Boulder, Colorado 80305, United States; Department of Physics, University of Colorado Boulder, Boulder, Colorado 80309, United States*

Geoffrey S. D. Beach − *Department of Materials Science and Engineering, Massachusetts Institute of Technology, Cambridge, Massachusetts 02139, United States*

Complete contact information is available at: https://pubs.acs.org/10.1021/acsami.3c14706

Author Contributions

[‖]T.F. and B.K. contributed equally to this work.

Notes

The authors declare no competing financial interest.

ACKNOWLEDGMENTS

The authors acknowledge support from NSF Grant No. DMR2028199, from SMART, an nCORE Center supported by SRC and NIST, and from the DARPA TEE program. Shared experimental facilities supported by the NSF MRSEC Program, Grant No. DMR1419807 were used.

REFERENCES

(1) Stoica, M.; Lo, C. S. P-Type Zinc Oxide Spinels: Application to Transparent Conductors and Spintronics. *New J. Phys.* **2014**, *16* (5), No. 055011.

(2) Thakur, P.; Chahar, D.; Taneja, S.; Bhalla, N.; Thakur, A. A Review on MnZn Ferrites: Synthesis, Characterization and Applications. *Ceram. Int.* **2020**, *46* (10, Part B), 15740−15763.

(3) Zhou, H.-A.; Xu, T.; Bai, H.; Jiang, W. Efficient Spintronics with Fully Compensated Ferrimagnets. *J. Phys. Soc. Jpn.* **2021**, *90* (8), No. 081006.

(4) Yang, Y.; Liu, T.; Bi, L.; Deng, L. Recent Advances in Development of Magnetic Garnet Thin Films for Applications in Spintronics and Photonics. *J. Alloys Compd.* **2021**, *860*, No. 158235.

(5) Khurana, B.; Bauer, J. J.; Zhang, P.; Safi, T.; Chou, C.-T.; Hou, J. T.; Fakhrul, T.; Fan, Y.; Liu, L.; Ross, C. A. Magnetism and Spin Transport in Platinum/Scandium-Substituted Terbium Iron Garnet Heterostructures. *Phys. Rev. Mater.* **2021**, *5* (8), No. 084408.

(6) Geller, S.; Williams, H. J.; Sherwood, R. C.; Remeika, J. P.; Espinosa, G. P. Magnetic Study of the Lighter Rare-Earth Ions in the Iron Garnets. *Phys. Rev.* **1963**, *131* (3), 1080−1082.

(7) Geller, S.; Remeika, J. P.; Sherwood, R. C.; Williams, H. J.; Espinosa, G. P. Magnetic Study of the Heavier Rare-Earth Iron Garnets. *Phys. Rev.* **1965**, *137* (3A), A1034−A1038.

(8) Pearson, R. F. Magnetocrystalline Anisotropy of Rare-Earth Iron Garnets. In *Proceedings of the Seventh Conference on Magnetism and Magnetic Materials*; Osborn, J. A., Ed.; Springer US: Boston, MA, 1962; pp 1236−1242.

(9) Iida, S. Magnetostriction Constants of Rare Earth Iron Garnets. *J. Phys. Soc. Jpn.* **1967**, *22* (5), 1201−1209.

(10) Chang, H.; Li, P.; Zhang, W.; Liu, T.; Hoffmann, A.; Deng, L.; Wu, M. Nanometer-Thick Yttrium Iron Garnet Films With Extremely Low Damping. *IEEE Magn. Lett.* **2014**, *5*, 6700104.

(11) Rosenberg, E. R.; Beran, L.; Avci, C. O.; Zeledon, C.; Song, B.; Gonzalez-Fuentes, C.; Mendil, J.; Gambardella, P.; Veis, M.; Garcia, C.; Beach, G. S. D.; Ross, C. A. Magnetism and Spin Transport in Rare-Earth-Rich Epitaxial Terbium and Europium Iron Garnet Films. *Phys. Rev. Mater.* **2018**, *2* (9), No. 094405.

(12) Bauer, J. J.; Rosenberg, E. R.; Kundu, S.; Mkhoyan, K. A.; Quarterman, P.; Grutter, A. J.; Kirby, B. J.; Borchers, J. A.; Ross, C. A. Dysprosium Iron Garnet Thin Films with Perpendicular Magnetic Anisotropy on Silicon. *Adv. Electron. Mater.* **2020**, *6* (1), No. 1900820.

(13) Bauer, J. J.; Rosenberg, E. R.; Ross, C. A. Perpendicular Magnetic Anisotropy and Spin Mixing Conductance in Polycrystalline

Europium Iron Garnet Thin Films. *Appl. Phys. Lett.* **2019**, *114* (5), No. 052403.
(14) Rosenberg, E. R.; Litzius, K.; Shaw, J. M.; Riley, G. A.; Beach, G. S. D.; Nembach, H. T.; Ross, C. A. Magnetic Properties and Growth-Induced Anisotropy in Yttrium Thulium Iron Garnet Thin Films. *Adv. Electron. Mater.* **2021**, *7* (10), No. 2100452.
(15) Linzen, D.; Bornmann, S.; Görnert, P.; Hergt, R.; Pfeiffer, H.; Schüppel, W.; Voigt, F.; Wendt, M. Growth-Induced Magnetic Anisotropy of (Sm, Ga)-Substituted YIG Films Grown on 111 Substrates. *Phys. Status Solidi A* **1977**, *43* (1), 277−281.
(16) Avci, C. O.; Quindeau, A.; Pai, C.-F.; Mann, M.; Caretta, L.; Tang, A. S.; Onbasli, M. C.; Ross, C. A.; Beach, G. S. D. Current-Induced Switching in a Magnetic Insulator. *Nat. Mater.* **2017**, *16* (3), 309−314.
(17) Yamahara, H.; Mikami, M.; Seki, M.; Tabata, H. Epitaxial Strain-Induced Magnetic Anisotropy in Sm3Fe5O12 Thin Films Grown by Pulsed Laser Deposition. *J. Magn. Magn. Mater.* **2011**, *323* (23), 3143−3146.
(18) Kumar, N.; Kim, N. G.; Park, Y. A.; Hur, N.; Jung, J. H.; Han, K. J.; Yee, K. J. Epitaxial Growth of Terbium Iron Garnet Thin Films with Out-of-Plane Axis of Magnetization. *Thin Solid Films* **2008**, *516* (21), 7753−7757.
(19) Li, P.; Liu, T.; Chang, H.; Kalitsov, A.; Zhang, W.; Csaba, G.; Li, W.; Richardson, D.; DeMann, A.; Rimal, G.; Dey, H.; Jiang, J. S.; Porod, W.; Field, S. B.; Tang, J.; Marconi, M. C.; Hoffmann, A.; Mryasov, O.; Wu, M. Spin−Orbit Torque-Assisted Switching in Magnetic Insulator Thin Films with Perpendicular Magnetic Anisotropy. *Nat. Commun.* **2016**, *7* (1), 12688.
(20) Wu, C. N.; Tseng, C. C.; Lin, K. Y.; Cheng, C. K.; Yeh, S. L.; Fanchiang, Y. T.; Hong, M.; Kwo, J. High-Quality Single-Crystal Thulium Iron Garnet Films with Perpendicular Magnetic Anisotropy by off-Axis Sputtering. *AIP Adv.* **2018**, *8* (5), No. 055904.
(21) Quindeau, A.; Avci, C. O.; Liu, W.; Sun, C.; Mann, M.; Tang, A. S.; Onbasli, M. C.; Bono, D.; Voyles, P. M.; Xu, Y.; Robinson, J.; Beach, G. S. D.; Ross, C. A. Tm3Fe5O12/Pt Heterostructures with Perpendicular Magnetic Anisotropy for Spintronic Applications. *Adv. Electron. Mater.* **2017**, *3* (1), No. 1600376.
(22) Avci, C. O.; Rosenberg, E.; Baumgartner, M.; Beran, L.; Quindeau, A.; Gambardella, P.; Ross, C. A.; Beach, G. S. D. Fast Switching and Signature of Efficient Domain Wall Motion Driven by Spin-Orbit Torques in a Perpendicular Anisotropy Magnetic Insulator/Pt Bilayer. *Appl. Phys. Lett.* **2017**, *111* (7), No. 072406.
(23) Ciubotariu, O.; Semisalova, A.; Lenz, K.; Albrecht, M. Strain-Induced Perpendicular Magnetic Anisotropy and Gilbert Damping of Tm3Fe5O12 Thin Films. *Sci. Rep.* **2019**, *9* (1), 17474.
(24) Ding, S.; Ross, A.; Lebrun, R.; Becker, S.; Lee, K.; Boventer, I.; Das, S.; Kurokawa, Y.; Gupta, S.; Yang, J.; Jakob, G.; Kläui, M. Interfacial Dzyaloshinskii-Moriya Interaction and Chiral Magnetic Textures in a Ferrimagnetic Insulator. *Phys. Rev. B* **2019**, *100* (10), No. 100406.
(25) Zhu, L.; Ralph, D. C.; Buhrman, R. A. Effective Spin-Mixing Conductance of Heavy-Metal−Ferromagnet Interfaces. *Phys. Rev. Lett.* **2019**, *123* (5), No. 057203.
(26) Caretta, L.; Rosenberg, E.; Büttner, F.; Fakhrul, T.; Gargiani, P.; Valvidares, M.; Chen, Z.; Reddy, P.; Muller, D. A.; Ross, C. A.; Beach, G. S. D. Interfacial Dzyaloshinskii-Moriya Interaction Arising from Rare-Earth Orbital Magnetism in Insulating Magnetic Oxides. *Nat. Commun.* **2020**, *11* (1), 1090.
(27) Avci, C. O.; Rosenberg, E.; Caretta, L.; Büttner, F.; Mann, M.; Marcus, C.; Bono, D.; Ross, C. A.; Beach, G. S. D. Interface-Driven Chiral Magnetism and Current-Driven Domain Walls in Insulating Magnetic Garnets. *Nat. Nanotechnol.* **2019**, *14* (6), 561−566.
(28) Husain, S.; Fayet, O.; Prestes, N. F.; Collin, S.; Godel, F.; Jacquet, E.; Denneulin, T.; Dunin-Borkowski, R. E.; Thiaville, A.; Bibes, M.; Reyren, N.; Jaffrès, H.; Fert, A.; George, J.-M. Field-Free Switching of Perpendicular Magnetization in an Ultrathin Epitaxial Magnetic Insulator. *arXiv* **2023**, DOI: 10.48550/arXiv.2301.11469.
(29) Dzyaloshinsky, I. A Thermodynamic Theory of "Weak" Ferromagnetism of Antiferromagnetics. *J. Phys. Chem. Solids* **1958**, *4* (4), 241−255.
(30) Moriya, T. Anisotropic Superexchange Interaction and Weak Ferromagnetism. *Phys. Rev.* **1960**, *120* (1), 91−98.
(31) Bode, M.; Heide, M.; von Bergmann, K.; Ferriani, P.; Heinze, S.; Bihlmayer, G.; Kubetzka, A.; Pietzsch, O.; Blügel, S.; Wiesendanger, R. Chiral Magnetic Order at Surfaces Driven by Inversion Asymmetry. *Nature* **2007**, *447* (7141), 190−193.
(32) Fert, A.; Cros, V.; Sampaio, J. Skyrmions on the Track. *Nat. Nanotechnol.* **2013**, *8* (3), 152−156.
(33) Xu, Z.; Liu, Q.; Ji, Y.; Li, X.; Li, J.; Wang, J.; Chen, L. Strain-Tunable Interfacial Dzyaloshinskii−Moriya Interaction and Spin-Hall Topological Hall Effect in Pt/Tm3Fe5O12 Heterostructures. *ACS Appl. Mater. Interfaces* **2022**, *14* (14), 16791−16799.
(34) Fakhrul, T.; Huang, S.; Song, Y.; Khurana, B.; Beach, G. S. D.; Ross, C. A. Influence of Substrate on Interfacial Dzyaloshinskii-Moriya Interaction in Epitaxial Tm 3 Fe 5 O 12 Films. *Phys. Rev. B* **2023**, *107* (5), No. 054421.
(35) Vedmedenko, E. Y.; Kawakami, R. K.; Sheka, D. D.; Gambardella, P.; Kirilyuk, A.; Hirohata, A.; Binek, C.; Chubykalo-Fesenko, O.; Sanvito, S.; Kirby, B. J.; Grollier, J.; Everschor-Sitte, K.; Kampfrath, T.; You, C.-Y.; Berger, A. The 2020 Magnetism Roadmap. *J. Phys. Appl. Phys.* **2020**, *53* (45), 453001.
(36) Mangin, S.; Henry, Y.; Ravelosona, D.; Katine, J. A.; Fullerton, E. E. Reducing the Critical Current for Spin-Transfer Switching of Perpendicularly Magnetized Nanomagnets. *Appl. Phys. Lett.* **2009**, *94* (1), No. 012502.
(37) How, H.; O'Handley, R. C.; Morgenthaler, F. R. Soliton Theory for Realistic Magnetic Domain-Wall Dynamics. *Phys. Rev. B* **1989**, *40* (7), 4808−4817.
(38) Serga, A. A.; Chumak, A. V.; Hillebrands, B. YIG Magnonics. *J. Phys. Appl. Phys.* **2010**, *43* (26), No. 264002.
(39) Schmidt, G.; Hauser, C.; Trempler, P.; Paleschke, M.; Papaioannou, E. Th. Ultra Thin Films of Yttrium Iron Garnet with Very Low Damping: A Review. *Phys. Status Solidi B* **2020**, *257* (7), No. 1900644.
(40) Fu, J.; Hua, M.; Wen, X.; Xue, M.; Ding, S.; Wang, M.; Yu, P.; Liu, S.; Han, J.; Wang, C.; Du, H.; Yang, Y.; Yang, J. Epitaxial Growth of Y3Fe5O12 Thin Films with Perpendicular Magnetic Anisotropy. *Appl. Phys. Lett.* **2017**, *110* (20), 202403.
(41) Sellappan, P.; Tang, C.; Shi, J.; Garay, J. E. An Integrated Approach to Doped Thin Films with Strain-Tunable Magnetic Anisotropy: Powder Synthesis, Target Preparation and Pulsed Laser Deposition of Bi:YIG. *Mater. Res. Lett.* **2017**, *5* (1), 41−47.
(42) Lage, E.; Beran, L.; Quindeau, A. U.; Ohnoutek, L.; Kucera, M.; Antos, R.; Sani, S. R.; Dionne, G. F.; Veis, M.; Ross, C. A. Temperature-Dependent Faraday Rotation and Magnetization Reorientation in Cerium-Substituted Yttrium Iron Garnet Thin Films. *APL Mater.* **2017**, *5* (3), No. 036104.
(43) Yang, Q.-H.; Zhang, H.-W.; Wen, Q.-Y.; Liu, Y.-L.; Xiao, J. Q. Tuning Magnetic Properties of Yttrium Iron Garnet Film with Oxygen Partial Pressure in Sputtering and Annealing Process. *J. Appl. Phys.* **2009**, *105* (7), No. 07A501.
(44) Soumah, L.; Beaulieu, N.; Qassym, L.; Carrétéro, C.; Jacquet, E.; Lebourgeois, R.; Ben Youssef, J.; Bortolotti, P.; Cros, V.; Anane, A. Ultra-Low Damping Insulating Magnetic Thin Films Get Perpendicular. *Nat. Commun.* **2018**, *9* (1), 3355.
(45) Fakhrul, T.; Khurana, B.; Nembach, H. T.; Shaw, J. M.; Fan, Y.; Riley, G. A.; Liu, L.; Ross, C. A. Substrate-Dependent Anisotropy and Damping in Epitaxial Bismuth Yttrium Iron Garnet Thin Films. *Adv. Mater. Interfaces* **2023**, *10* (30), No. 2300217.
(46) Crossley, S.; Quindeau, A.; Swartz, A. G.; Rosenberg, E. R.; Beran, L.; Avci, C. O.; Hikita, Y.; Ross, C. A.; Hwang, H. Y. Ferromagnetic Resonance of Perpendicularly Magnetized Tm3Fe5O12/Pt Heterostructures. *Appl. Phys. Lett.* **2019**, *115* (17), 172402.

(47) Caretta, L.; Oh, S.-H.; Fakhrul, T.; Lee, D.-K.; Lee, B. H.; Kim, S. K.; Ross, C. A.; Lee, K.-J.; Beach, G. S. D. Relativistic Kinematics of a Magnetic Soliton. *Science* **2020**, *370* (6523), 1438−1442.
(48) Vélez, S.; Ruiz-Gómez, S.; Schaab, J.; Gradauskaite, E.; Wörnle, M. S.; Welter, P.; Jacot, B. J.; Degen, C. L.; Trassin, M.; Fiebig, M.; Gambardella, P. Current-Driven Dynamics and Ratchet Effect of Skyrmion Bubbles in a Ferrimagnetic Insulator. *Nat. Nanotechnol.* **2022**, *17* (8), 834−841.
(49) Kahl, S.; Grishin, A. M. Enhanced Faraday Rotation in All-Garnet Magneto-Optical Photonic Crystal. *Appl. Phys. Lett.* **2004**, *84* (9), 1438−1440.
(50) Rastogi, A. C.; Moorthy, V. N. Magnetic Properties of Multilayers of Nano Thin Co,Ce-Doped and Undoped Yttrium Iron Garnet Films for Magneto-Optic Applications. *Mater. Sci. Eng., B* **2002**, *95* (2), 131−136.
(51) Fakhrul, T.; Tazlaru, S.; Beran, L.; Zhang, Y.; Veis, M.; Ross, C. A. Magneto-Optical Bi:YIG Films with High Figure of Merit for Nonreciprocal Photonics. *Adv. Opt. Mater.* **2019**, *7* (13), No. 1900056.
(52) Geller, S.; Gilleo, M. A. The Crystal Structure and Ferrimagnetism of Yttrium-Iron Garnet, Y3Fe2(FeO4)3. *J. Phys. Chem. Solids* **1957**, *3* (1), 30−36.
(53) *Magnetic and Other Properties of Oxides and Related Compounds · Part A: Garnets and Perovskites*; Hellwege, K.-H.; Hellwege, A. M., Eds.; Landolt-Börnstein - Group III Condensed Matter; Springer-Verlag: Berlin/Heidelberg, 1978; Vol. *12a*.
(54) Manuilov, S. A.; Khartsev, S. I.; Grishin, A. M. Pulsed Laser Deposited Y3Fe5O12 Films: Nature of Magnetic Anisotropy I. *J. Appl. Phys.* **2009**, *106* (12), 123917.
(55) Manuilov, S. A.; Grishin, A. M. Pulsed Laser Deposited Y3Fe5O12 Films: Nature of Magnetic Anisotropy II. *J. Appl. Phys.* **2010**, *108* (1), No. 013902.
(56) Lee, A. J.; Ahmed, A. S.; McCullian, B. A.; Guo, S.; Zhu, M.; Yu, S.; Woodward, P. M.; Hwang, J.; Hammel, P. C.; Yang, F. Interfacial Rashba-Effect-Induced Anisotropy in Nonmagnetic-Material–Ferrimagnetic-Insulator Bilayers. *Phys. Rev. Lett.* **2020**, *124* (25), No. 257202.
(57) Büttner, F.; Mawass, M. A.; Bauer, J.; Rosenberg, E.; Caretta, L.; Avci, C. O.; Gräfe, J.; Finizio, S.; Vaz, C. A. F.; Novakovic, N.; Weigand, M.; Litzius, K.; Förster, J.; Träger, N.; Groß, F.; Suzuki, D.; Huang, M.; Bartell, J.; Kronast, F.; Raabe, J.; Schütz, G.; Ross, C. A.; Beach, G. S. D. Thermal Nucleation and High-Resolution Imaging of Submicrometer Magnetic Bubbles in Thin Thulium Iron Garnet Films with Perpendicular Anisotropy. *Phys. Rev. Mater.* **2020**, *4* (1), No. 011401.
(58) Hansen, P.; Witter, K.; Tolksdorf, W. Magnetic and Magneto-Optic Properties of Lead- and Bismuth-Substituted Yttrium Iron Garnet Films. *Phys. Rev. B* **1983**, *27* (11), 6608−6625.
(59) Nembach, H. T.; Silva, T. J.; Shaw, J. M.; Schneider, M. L.; Carey, M. J.; Maat, S.; Childress, J. R. Perpendicular Ferromagnetic Resonance Measurements of Damping and Lande g - Factor in Sputtered (Co2Mn)1−xGex Thin Films. *Phys. Rev. B* **2011**, *84* (5), No. 054424.
(60) Ding, Y.; Klemmer, T. J.; Crawford, T. M. A Coplanar Waveguide Permeameter for Studying High-Frequency Properties of Soft Magnetic Materials. *J. Appl. Phys.* **2004**, *96* (5), 2969−2972.
(61) Neudecker, I.; Woltersdorf, G.; Heinrich, B.; Okuno, T.; Gubbiotti, G.; Back, C. H. Comparison of Frequency, Field, and Time Domain Ferromagnetic Resonance Methods. *J. Magn. Magn. Mater.* **2006**, *307* (1), 148−156.
(62) Kalarickal, S. S.; Krivosik, P.; Wu, M.; Patton, C. E.; Schneider, M. L.; Kabos, P.; Silva, T. J.; Nibarger, J. P. Ferromagnetic Resonance Linewidth in Metallic Thin Films: Comparison of Measurement Methods. *J. Appl. Phys.* **2006**, *99* (9), No. 093909.
(63) Hillebrands, B. Progress in Multipass Tandem Fabry−Perot Interferometry: I. A Fully Automated, Easy to Use, Self-Aligning Spectrometer with Increased Stability and Flexibility. *Rev. Sci. Instrum.* **1999**, *70* (3), 1589−1598.
(64) Nembach, H. T.; Shaw, J. M.; Weiler, M.; Jué, E.; Silva, T. J. Linear Relation between Heisenberg Exchange and Interfacial Dzyaloshinskii−Moriya Interaction in Metal Films. *Nat. Phys.* **2015**, *11* (10), 825−829.
(65) Ma, X.; Yu, G.; Tang, C.; Li, X.; He, C.; Shi, J.; Wang, K. L.; Li, X. Interfacial Dzyaloshinskii-Moriya Interaction: Effect of $5d$ Band Filling and Correlation with Spin Mixing Conductance. *Phys. Rev. Lett.* **2018**, *120* (15), No. 157204.
(66) Damon, R. W.; Eshbach, J. R. Magnetostatic Modes of a Ferromagnet Slab. *J. Phys. Chem. Solids* **1961**, *19* (3), 308−320.
(67) Ding, S.; Baldrati, L.; Ross, A.; Ren, Z.; Wu, R.; Becker, S.; Yang, J.; Jakob, G.; Brataas, A.; Kläui, M. Identifying the Origin of the Nonmonotonic Thickness Dependence of Spin-Orbit Torque and Interfacial Dzyaloshinskii-Moriya Interaction in a Ferrimagnetic Insulator Heterostructure. *Phys. Rev. B* **2020**, *102* (5), No. 054425.
(68) Caretta, L.; Mann, M.; Büttner, F.; Ueda, K.; Pfau, B.; Günther, C. M.; Hessing, P.; Churikova, A.; Klose, C.; Schneider, M.; Engel, D.; Marcus, C.; Bono, D.; Bagschik, K.; Eisebitt, S.; Beach, G. S. D. Fast Current-Driven Domain Walls and Small Skyrmions in a Compensated Ferrimagnet. *Nat. Nanotechnol.* **2018**, *13* (12), 1154−1160.
(69) Woo, S.; Litzius, K.; Krüger, B.; Im, M.-Y.; Caretta, L.; Richter, K.; Mann, M.; Krone, A.; Reeve, R. M.; Weigand, M.; Agrawal, P.; Lemesh, I.; Mawass, M.-A.; Fischer, P.; Kläui, M.; Beach, G. S. D. Observation of Room-Temperature Magnetic Skyrmions and Their Current-Driven Dynamics in Ultrathin Metallic Ferromagnets. *Nat. Mater.* **2016**, *15* (5), 501−506.
(70) Moreau-Luchaire, C.; Moutafis, C.; Reyren, N.; Sampaio, J.; Vaz, C. A. F.; Van Horne, N.; Bouzehouane, K.; Garcia, K.; Deranlot, C.; Warnicke, P.; Wohlhüter, P.; George, J.-M.; Weigand, M.; Raabe, J.; Cros, V.; Fert, A. Additive Interfacial Chiral Interaction in Multilayers for Stabilization of Small Individual Skyrmions at Room Temperature. *Nat. Nanotechnol.* **2016**, *11* (5), 444−448.

https://doi.org/10.1021/acsami.3c14706
ACS Appl. Mater. Interfaces XXXX, XXX, XXX−XXX